

# Characterisation and Modelling of the Indoor Pseudorange Error using Low Cost Receivers

Thomas Jost, *German Aerospace Center (DLR)*  
Mohammed Khider, *German Aerospace Center (DLR)*  
Elena Abdo Sánchez, *German Aerospace Center (DLR)*

## BIOGRAPHY

Thomas Jost received a Diploma degree (FH) 2001 in Electrical Engineering from University of Applied Science Wiesbaden, Germany and Diploma degree 2003 in Electrical Engineering and Information Technology from Technical University of Darmstadt, Germany. From 2003 to 2006 he held a research assistant position at Signal Processing Group at TU Darmstadt. Since 2006 he is a member of the scientific staff of the Institute of Communications and Navigation at the German Aerospace Center.

Mohammed Khider received his master degree in Communications Technology from the University Of Ulm, Germany. He obtained his B.Sc. degree in Electrical Engineering/Communications Track from the UAE University, United Arab Emirates. He is currently with the German Aerospace Center and a PhD student at the University of Ulm. His research interests are navigation, multisensor fusion, mobility models, signal processing and context aware services.

Elena Abdo Sánchez is currently finishing her master thesis of Telecommunications Engineering, which was done in the Institute of Communications and Navigation at the German Aerospace Center. She has studied Telecommunications Engineering at the University of Málaga, Spain (started in 2004). One of the university years (2007-2008) was done at the University of Ulm, Germany.

## ABSTRACT

Indoor navigation is one of the emerging topics in the last years due to the growing demand of consumers looking for location based services available everywhere. Sensor fusion can solve indoor localisation with an acceptable accuracy. Global Navigation Satellite Systems (GNSSs) are important sensors for positioning in outdoor navigation as it provides long-term accuracy without the need of a local infrastructure and are globally available. However, in indoor environments satellite signals are difficult to receive due to the attenuation caused by building materials. Additionally, diffraction and a diffuse multipath in general cause range estimation errors and accordingly, impede an accurate localisation by GNSSs in such environments.

In this contribution we characterise and build a model for the ranging error of the Global Positioning System (GPS) mainly caused by multipath propagation and diffraction/refraction. Since the room and its major fixtures such as furniture and windows, as well as the surrounding building(s), are largely static, a temporal correlation of the pseudorange error measured at a fixed point is to be expected. This is taking into consideration that the satellites motion is too slow to cause sudden channel changes due to changes in the incoming wave angles. Additionally, a certain spatial correlation could be expected as reflecting objects such as walls, will remain in their positions. However, due to the interaction of different reflected waves, a small change in receiver position might degrade the spatial error covariance.

## I. INTRODUCTION

The proliferation of mobile devices and the availability of information rise the demand of services fitting the user's position, and thus making location awareness of the devices increasingly important. Outdoor localisation, up to a certain precision, can be obtained using GNSS, like the available GPS or the future Galileo system. However, in indoor environments, GNSS accuracy is drastically reduced due to diffraction, refraction, multipath and low received signal power resulting from attenuation of building materials. Therefore, research in indoor positioning is widely spread into different methods and sensor systems. Most work on this topic is on infrastructure based solutions such as radio frequency identification (RFID) [1] or WLAN [2]. The difficulty for these types of location systems is the need of infrastructure provided by the indoor environment, which limits the availability or increases the cost as the facility has to be maintained and managed.

Non-infrastructure based positioning systems are also available, such as the foot-mounted inertial system [3]. Other sensors like barometer or compass may help in terms of sensor fusion [4]. These solutions do not need any infrastructure and can therefore be used everywhere. The disadvantage of non-infrastructure based navigation systems is the use of a local coordinate system, which has to be mapped to a global one in order to use available information, like maps. Therefore, a reference to a global coordinate system at the start is normally needed, which implies directly a long-term inaccuracy due to error propagation, if a synchronisation

between the local and the global coordinate systems cannot be done from time-to-time. Hence, linking infrastructure-less solutions with a globally working positioning system, like GPS, is advantageous even if it is done on an irregular basis.

Low cost GPS receivers available on the mass market are able to track satellite signals down to a received signal strength of  $-160$  dBm. With these high sensitivity devices, receiving (i.e. acquiring) GNSS signals indoors becomes possible. But still, the building material used, the type of construction and the rooms layout have a great influence on the signal propagation, i.e. on estimation accuracy. Attenuation caused by thick concrete walls increases the estimation variance due to a lower signal-to-noise ratio. On the other hand, multipath and diffraction effects cause a bias in the delay-locked loop (DLL) estimator. In order to mitigate errors due to the signal propagation, in the framework of recursive Bayesian estimation used in sensor fusion, models which accurately describe the error propagation over time and space have to be found and incorporated. But how to find such models? One attempt that has been pursued in this contribution is to measure the pseudorange error and characterise it. First results on the measurements have been published in [5].

In this paper, the performed measurements are described in Section II, followed by an error analysis in Section III and the results in Section IV. At the end, in Section V, a summary and an outlook to future work will be given.

## II. MEASUREMENTS

For completeness we will shortly describe the measurements performed as done in [5].

Measurements were carried out in an entry hall of a three-story building using five low cost GPS receivers with SiRF III chipsets. We assume that the receivers will have the same behaviour in pseudorange errors trends, as they share the same chipset and therefore, the same estimation algorithms. The entry hall was chosen because it allowed a separation of several meters between the receivers without blockage by walls. Receivers were arranged in a cross form (as shown in Fig. 1) at five different locations inside the entry hall. At each of the location  $P_1$  to  $P_5$  (shown in Fig. 2) the distance  $d$  between the outer four receivers to the middle one was varied between 20 cm and 5 m in steps of 20 cm, 60 cm, 120 cm and 500 cm. For each distance  $d$ , we measured simultaneously GPS L1 C/A pseudoranges from each receiver for all the satellites in view. Measurements were taken with a period of 1 s for at least 45 minutes at each location  $P_i$ ,  $i = 1, \dots, 5$  and given distance  $d$ . It has to be noted that the position of each receiver was precisely measured using a Leica tachymeter system TPS1200. In order to compensate for atmospheric and second order relativistic effects, we placed a receiver on the roof of a nearby house. This receiver record GPS L1 C/A pseudoranges at a known location.

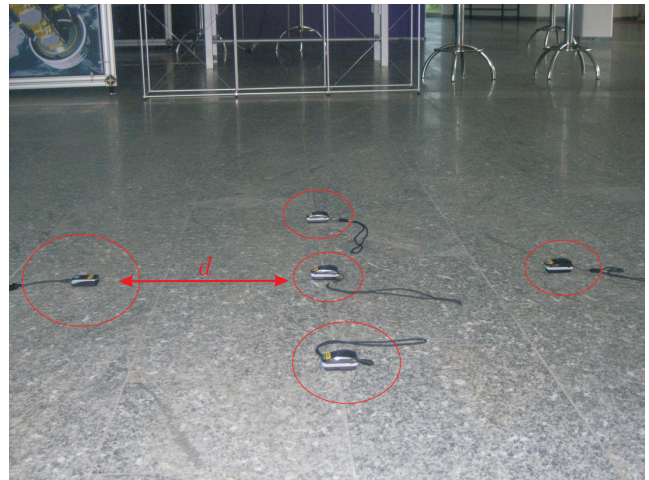


Fig. 1. Measurement setup using a cross form, with one receiver in the middle and four outer receivers, with spacing  $d$ .

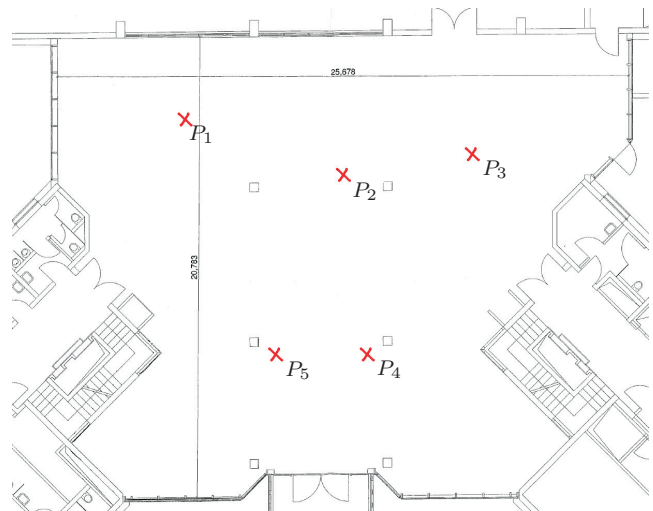


Fig. 2. Measurement locations  $P_1$  to  $P_5$  inside the entry hall.

## III. ANALYSIS

According to [6] the measured pseudorange at time  $t$  to satellite  $i$  can be modeled as

$$\rho_i(t) = |x_i(t - \tau) - x_u(t)| + cb_u(t) - cb_i(t - \tau) + I_i(t) + T_i(t) + \epsilon_i(t) \quad (1)$$

where  $\tau$  stands for the propagation delay,  $x_i(t)$  the position of satellite  $i$  at time  $t$ ,  $x_u(t)$  the receiver position vector,  $b_u(t)$  the user clock bias,  $b_i(t)$  the satellite clock bias,  $I_i(t)$  and  $T_i(t)$  the modeled range errors caused by ionosphere and troposphere, respectively, and  $c$  the speed of light.  $\epsilon_i(t)$  describes a residual term that is caused by atmospheric model errors, as well as, satellite position uncertainty, unmodeled relativistic effects, multipath propagation, receiver clock estimation errors and white receiver noise (interference effects are ignored here).

Therefore  $\epsilon_i(t)$  can be expressed as

$$\begin{aligned} \epsilon_i(t) &= \Delta I_i(t) + \Delta T_i(t) + \Delta x_i(t - \tau) + \Delta r_i(t) \\ &\quad + m_i(t) + w_i(t) + c\Delta b_u(t) \end{aligned} \quad (2)$$

where  $\Delta I_i(t)$  and  $\Delta T_i(t)$  stand for ionosphere and troposphere model errors respectively,  $\Delta x_i(t - \tau)$  is the satellite position error,  $\Delta r_i(t)$  is the unmodeled relativistic effect,  $m_i(t)$  describes the error introduced by multipath,  $w_i(t)$  is the white receiver noise and  $c\Delta b_u(t)$  is the error of the clock bias estimation. As  $x_i(t - \tau)$  and  $cb_i(t - \tau)$  can be calculated out of the navigation message,  $x_u(t)$  is measured precisely by a tachymeter and  $I_i(t)$ ,  $T_i(t)$  and  $cb_u(t)$  are calculated when solving for a position (using the navigation equation). We may write the final residual between pseudorange measure  $\rho_i(t)$ , and its estimate using the accurate user position as follows:

$$\begin{aligned} \epsilon_i(t) &= \rho_i(t) - |x_i(t - \tau) - x_u(t)| \\ &\quad - cb_u(t) + cb_i(t - \tau) - I_i(t) - T_i(t), \end{aligned} \quad (3)$$

where the residual  $\epsilon_i(t)$  expresses all errors described in eq. (2). As described in Section II, a second receiver served as a reference is placed on the roof to compensate for atmospheric and relativistic effects as well as satellite position uncertainty and clock errors. Calculating the residual  $\epsilon_{i,r}(t)$  for the reference receiver and taking the difference to  $\epsilon_i(t)$ , the result may be expressed as:

$$\begin{aligned} \epsilon_i(t) &= \epsilon_i(t) - \epsilon_{i,r}(t) \\ &= m_i(t) + w_i(t) + c\Delta b_u(t) - w_{i,r}(t) - c\Delta b_r(t), \end{aligned} \quad (4)$$

where  $w_{i,r}(t)$  and  $c\Delta b_r(t)$  are the white noise and the clock estimation error of the reference receiver, respectively. We made the assumption that a multipath error at the reference receiver is not present or negligible, as the receiver is positioned on the roof with open-sky condition. Further, we assumed that the distance between indoor receivers and the reference receiver is close enough such that the azimuth and elevation angles from receiver to satellites do not differ significantly. This approach can be classified as differential GPS [7], and may simulate corrections coming via an assisted GNSS connection. Additionally, we classify  $w_{i,r}(t)$  and  $c\Delta b_r(t)$  as marginal compared to  $m_i(t) + w_i(t) + c\Delta b_u(t)$ , as the reference receiver is placed outside in a multipath-free open-sky condition such that  $\epsilon_i(t)$  reduces to:

$$\epsilon_i(t) \approx m_i(t) + w_i(t) + c\Delta b_u(t). \quad (5)$$

In the analysis described further, we denote  $\epsilon_{k,i}(t)$  as the pseudorange error seen in the measurement  $k$  to satellite  $i$ , where  $k$  is an incremental number representing all locations ( $P_1$  to  $P_5$ ) and receivers. In the following, the statistical analysis is split into temporal and spatial analysis.

- The temporal characterisation shall give rise to a model of the pseudorange error, when a receiver is static (in location).
- The spatial characterisation shall result in a model, when the receiver is in motion.

### A. Temporal Characterisation

To analyse the temporal characteristics of the pseudorange error  $\epsilon_{k,i}(t)$ , a covariance analysis was performed. For simplicity, we will denote the pseudorange error as  $\epsilon_j(t)$  in this subsection, where  $\epsilon_j(t)$  stands for a pseudorange error sequence of consecutive time points of at least 150 s length. The sample covariance  $c_j(l)$  for  $\epsilon_j(t)$  can be expressed as

$$c_j(l) = E_t[(\epsilon_j(t+l) - E_t[\epsilon_j(t)]) (\epsilon_j(t) - E_t[\epsilon_j(t)])], \quad (6)$$

where  $E_x[\cdot]$  represents the sample mean over  $x$ . Assuming stationarity, the mean sample covariance  $c_{\epsilon\epsilon}(l)$  can be calculated as:

$$c_{\epsilon\epsilon}(l) = E_j[c_j(l)]. \quad (7)$$

Fig. 3 represents the normalised mean sample covariance over time difference  $l$ , which shows an exponential behaviour with a very long decaying tail. In [8] a similar result was

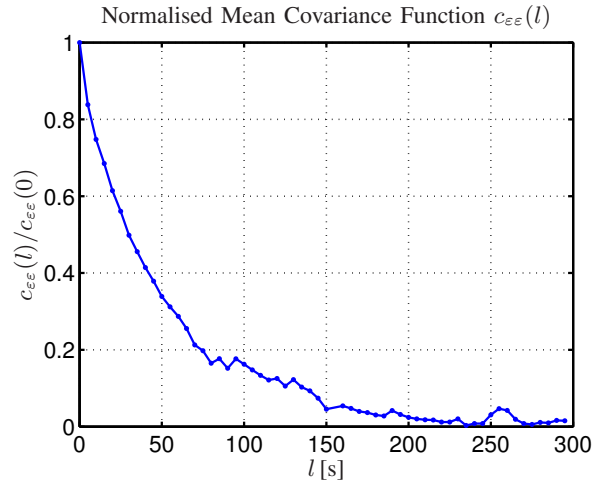


Fig. 3. Normalised version of the mean covariance function  $c_{\epsilon\epsilon}(l)$  calculated according to eq. (7).

found independently, except that a sinc function has been assumed for the shape. To model an exponentially decaying covariance, an autoregressive (AR) process is an appropriate choice [9]. An AR process  $x(t)$  is mathematically described as the output of a  $N$ th order all-pole filter with parameters  $a_n$ , with  $n = 1, \dots, N$ , driven by an independent identically distributed (i.i.d.) noise process  $v(t)$ . The AR process can be expressed as follows:

$$x(t) = \sum_{n=1}^N a_n x(t-n) + v(t). \quad (8)$$

To determine the model order  $N$  describing  $\epsilon_j(t)$  as an AR process, the minimum description length (MDL) [9] has been utilised. According to this criterion (using  $c_{\epsilon\epsilon}(l)$ ), a model order of  $N = 2$  has been sufficient to describe  $\epsilon_j(t)$  as an AR process. The same result has been found by applying the Bayesian information criterion (BIC) to individual sequences of  $\epsilon_j(t)$ .

To verify the model, the pseudorange error sequence sample

$\varepsilon_{j_0}(t)$  shown in Fig. 4 has been whitened using a finite impulse response filter, which is inverse to the estimated all-pole filter of order 2 in eq. (8). The result is shown in Fig. 5. It shows

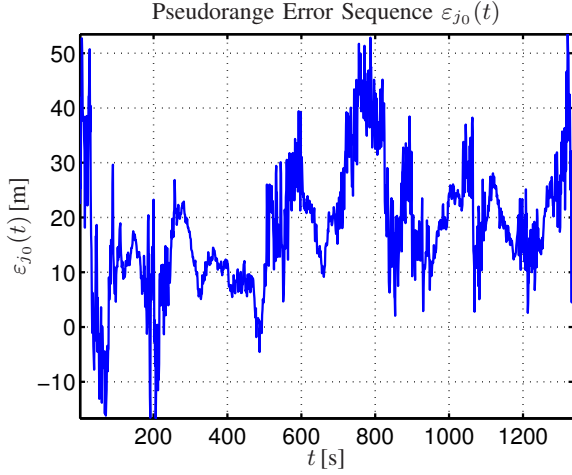


Fig. 4. Pseudorange error sequence  $\varepsilon_{j_0}(t)$  measured by a receiver located at  $P_1$ .

the estimated driving noise process  $\hat{v}_{j_0}(t)$ , which should be i.i.d. if the model assumption of a second order AR process is adequate. For verification, Fig. 6 shows the sample covariance

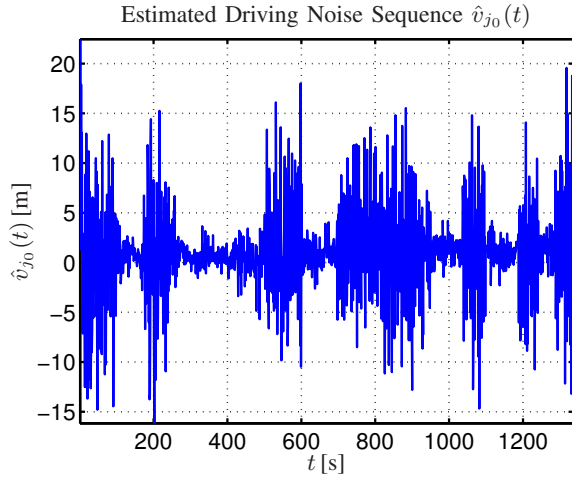


Fig. 5. Estimated driving noise sequence  $\hat{v}_{j_0}(t)$  obtained by whitening the pseudorange error sequence  $\varepsilon_{j_0}(t)$  shown in Fig. 4. A second order AR process is assumed for  $\varepsilon_{j_0}(t)$ .

function of  $\hat{v}_{j_0}(t)$  denoted as  $c_{\hat{v}\hat{v}}(l)$ . It displays a clear peak at  $l = 0$ , which confirms  $\hat{v}_{j_0}(t)$  to be i.i.d. and verifies the model assumption. In the appendix, the same derivation for another pseudorange error sequence  $\varepsilon_{k_1}(t)$ , measured at a different location by a different receiver is shown, confirming the model assumption.

The next step is to model the i.i.d. noise process  $v_j(t)$ . Looking at Fig. 5, the driving noise  $v_{j_0}(t)$  seem to be non-Gaussian. One way to model a non-Gaussian probability density function (pdf) is using a Gaussian Mixture Model

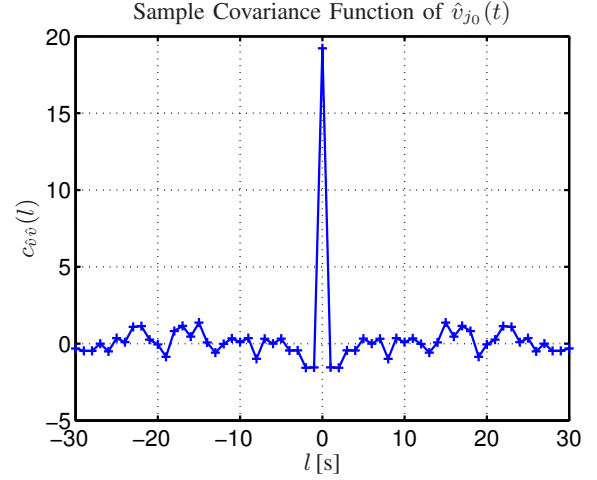


Fig. 6. Sample covariance function of  $\hat{v}_{j_0}(t)$  shown in Fig. 5.

(GMM). A GMM of order  $K$  (GMM( $K$ )) is defined as the sum of weighted normal distributions:

$$f(x) = \sum_{k=1}^K p_k \mathcal{N}(\mu_k, \sigma_k), \quad \text{with } \sum_{k=1}^K p_k = 1, \quad (9)$$

where  $\mathcal{N}(\mu_k, \sigma_k)$  represents a normal distribution with mean  $\mu_k$  and standard deviation  $\sigma_k$ , weighted by  $p_k$ ,  $k = 1, \dots, K$ . In general, a GMM can asymptotically represent an arbitrary shaped pdf. For simplicity, and being inspired by Fig. 5, we set  $K = 2$  for the further analysis. A non-parametric estimate of the pdf of  $\hat{v}_{j_0}(t)$  denoted as  $f(\hat{v}_{j_0})$  is shown in Fig. 7 together with its parametric estimate based on a GMM(2).

According to the described results, the temporal behaviour of

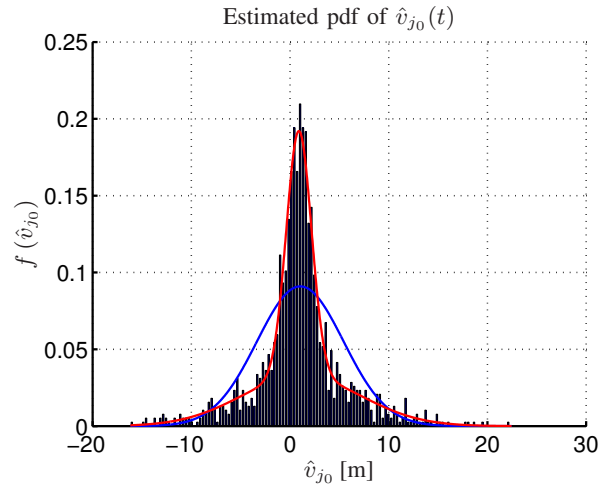


Fig. 7. Estimation of the pdf for  $\hat{v}_{j_0}(t)$  shown in Fig. 5. The blue curve visualises a Gaussian distribution having the same mean and variance as the data samples, while the red curve shows the parametric estimate based on a GMM(2).

$\varepsilon_j(t)$  is modelled as

$$\varepsilon_j(t) = a_{j,1} \varepsilon_j(t-1) + a_{j,2} \varepsilon_j(t-2) + v_j(t), \quad (10)$$

where  $v_j(t)$  is i.i.d. with pdf  $f(v_j)$  defined by

$$f(v_j) = p_j \mathcal{N}(\mu_{j,1}, \sigma_{j,1}) + (1 - p_j) \mathcal{N}(\mu_{j,2}, \sigma_{j,2}). \quad (11)$$

To get sufficient statistics for the model parameter set  $\Theta_j = [a_{j,1}, a_{j,2}, p_j, \mu_{j,1}, \sigma_{j,1}, \mu_{j,2}, \sigma_{j,2}]$ , the maximum likelihood based EMAX algorithm [10] was used to estimate  $\Theta_j$  for all sequences  $\varepsilon_j(t)$  that are having a minimum length of 150 s.

### B. Spatial Characterisation

Similar to the last section a covariance analysis has been performed to explore the spatial evolution of the pseudorange error  $\varepsilon_{k,i}(t)$  in a statistical manner. The spatial sample covariance function  $c_{\{k,l\},i}(d)$ . It is calculated as the sample cross-covariance between two pseudorange error sequences  $\varepsilon_{k,i}(t)$  and  $\varepsilon_{l,i}(t)$ , tracking the same satellite  $i$  at the same time  $t$ , but measured by two receivers which are spatially separated by distance  $d$ . Mathematically, the sample covariance is expressed as:

$$c_{\{k,l\},i}(d) = E_t[(\varepsilon_{l,i}(t) - E_t[\varepsilon_{l,i}(t)]) (\varepsilon_{k,i}(t) - E_t[\varepsilon_{k,i}(t)])]. \quad (12)$$

The mean spatial sample covariance function  $c_{\varepsilon\varepsilon}(d)$  is defined as the average over all sets  $\{k, l\}$  and all satellites  $i$  as:

$$c_{\varepsilon\varepsilon}(d) = E_{\{k,l\}}[E_i[c_{\{k,l\},i}(d)]] . \quad (13)$$

The normalised version of  $c_{\varepsilon\varepsilon}(d)$  is visualised in Fig. 8, which shows a fast decaying covariance function. From the figure we can notice that changing the position of the receiver seems to produce uncorrelated error samples.

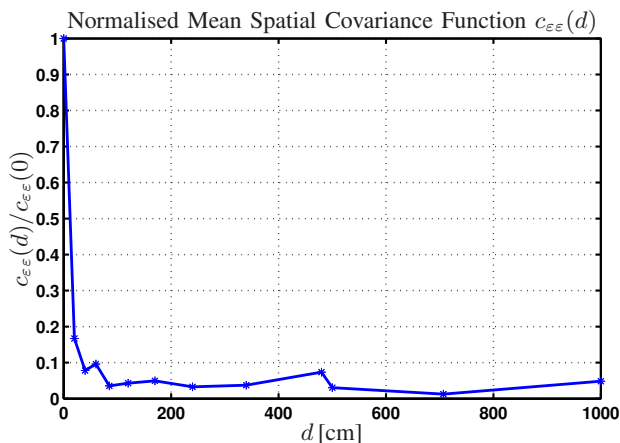


Fig. 8. Normalised version of the mean spatial covariance function  $c_{\varepsilon\varepsilon}(d)$  calculated according to eq. (13).

## IV. RESULTS

The results of the temporal characterisation have been found in terms of  $\Theta_j = [a_{j,1}, a_{j,2}, p_j, \mu_{j,1}, \sigma_{j,1}, \mu_{j,2}, \sigma_{j,2}]$  estimated by the EMAX algorithm. The first Gaussian of the GMM(2) is selected to be the one with a smaller standard deviation, such that  $\sigma_{j,1} \leq \sigma_{j,2}$ . The results for the individual parameters are shown in Table I with their mean and standard deviation values and in Fig. 9 to Fig. 15 in term of histograms.

TABLE I  
RESULTS OBTAINED BY USING EMAX.

	Parameter	Mean	Standard Deviation
AR	$a_{j,1}$	0.898	0.237
	$a_{j,2}$	0.06	0.213
GMM	$p_j$	0.576	0.283
	$\mu_{j,1}$	-0.172 m	3.486 m
	$\sigma_{j,1}$	1.447 m	1.285 m
	$\mu_{j,2}$	-0.155 m	1.97 m
	$\sigma_{j,2}$	5.316 m	2.976 m

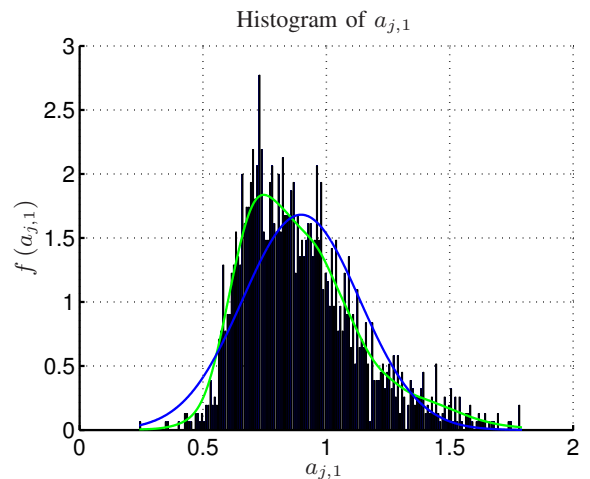


Fig. 9. Histogram of  $a_{j,1}$ . The green curve shows a Gaussian kernel estimate [11] and the blue curve represents a Gaussian distribution having the same mean and variance as the data samples.

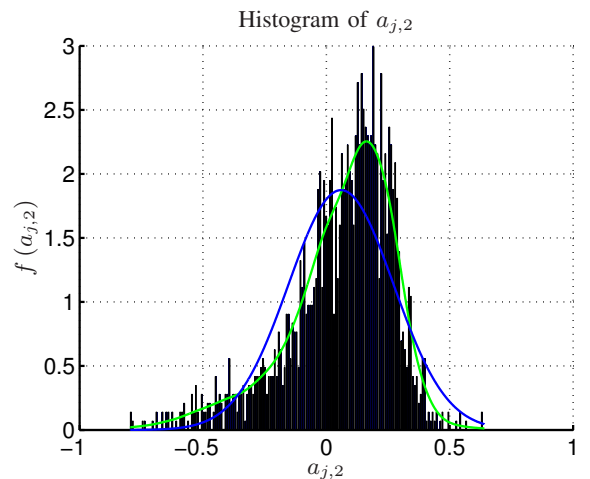


Fig. 10. Histogram of  $a_{j,2}$ . The green curve shows a Gaussian kernel estimate [11] and the blue curve represents a Gaussian distribution having the same mean and variance as the data samples.

The results suggest an AR process with quite stable coefficients as the variances of  $a_{j,1}$  and  $a_{j,2}$  are not very high. According to the mean of  $E_j[p_j] = 0.576$ , both normal distributions in the GMM(2) are approximately equally weighted.

This means that samples from the normal distribution with the

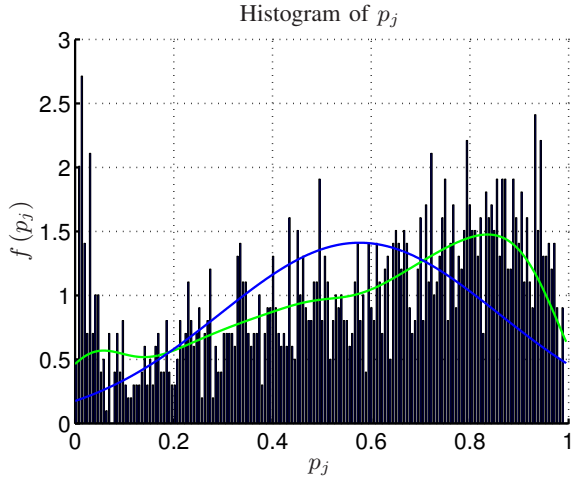


Fig. 11. Histogram of  $p_j$ . The green curve shows a Gaussian kernel estimate [11] and the blue curve represents a Gaussian distribution having the same mean and variance as the data samples.

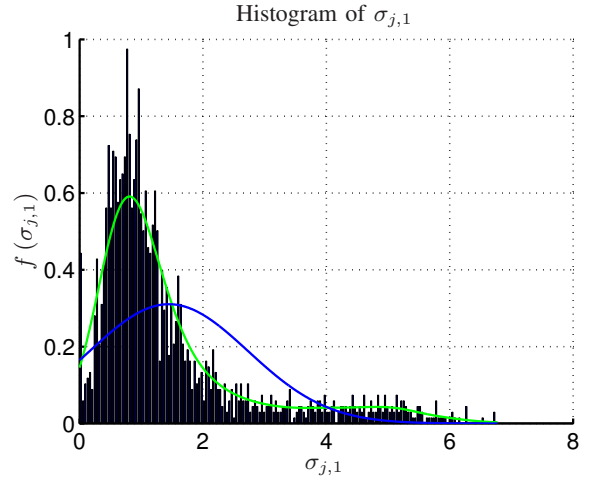


Fig. 13. Histogram of  $\sigma_{j,1}$ . The green curve shows a Gaussian kernel estimate [11] and the blue curve represents a Gaussian distribution having the same mean and variance as the data samples.

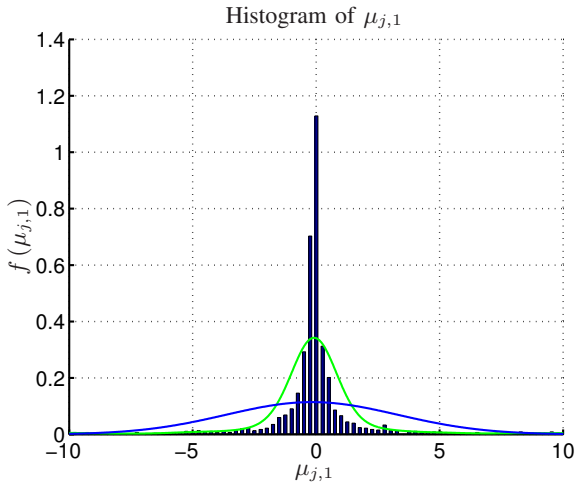


Fig. 12. Histogram of  $\mu_{j,1}$ . The green curve shows a Gaussian kernel estimate [11] and the blue curve represents a Gaussian distribution having the same mean and variance as the data samples.

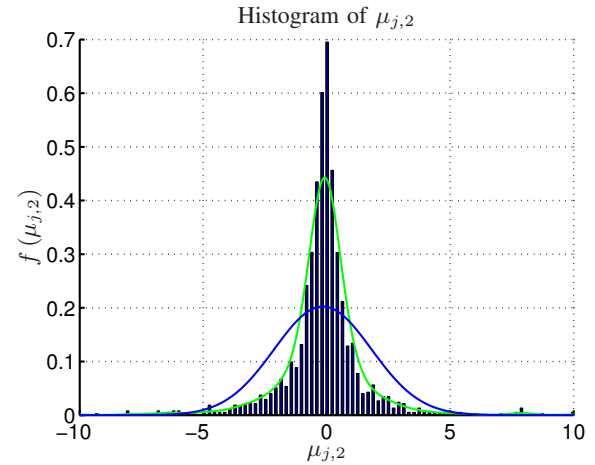


Fig. 14. Histogram of  $\mu_{j,2}$ . The green curve shows a Gaussian kernel estimate [11] and the blue curve represents a Gaussian distribution having the same mean and variance as the data samples.

lower variance denoted by index 1 are approximately equally occurring as samples from the normal distribution with index 2. Fig. 5 is a direct example of this, where parts of the time series with higher standard deviation are approximately as likely as parts with lower variance.

According to the sample distribution of the parameter  $p_j$  shown in Fig. 11, which shows a tendency towards a uniform distribution, all combinations of weightings between the two normal distributions in the GMM(2) occur in the measured data.

But what physical effect could cause this?

Seen from the receiver, the direction of arrival of the satellite's signal does not change fast, and accordingly the reflectors of multipath rays remain similar over short time, giving rise to temporal dependency of the multipath error in the delay-locked-loop (DLL) estimator.

According to the statistical evaluation in Section III, this dependency can be modelled as an AR process. Additionally, due to multipath, the pseudorange error may become non-Gaussian distributed with heavy tails which encourages the use of a GMM. Also, attenuations of signal strength happening for a certain time length due to fast fading or signal blockage by building materials could reduce the signal-to-noise ratio. This results in increasing the variance of the estimated pseudorange, which causes a heavy tailed noise.

Surely, signal processing algorithms and the hardware in the receiver will also have their share on the overall effect.

From Fig. 8, it can be assumed that the pseudorange error is uncorrelated after few centimeters of movement, which is consistent with [12]. According to [8], the decorrelation in space is even faster in small rooms. Assuming a pedestrian

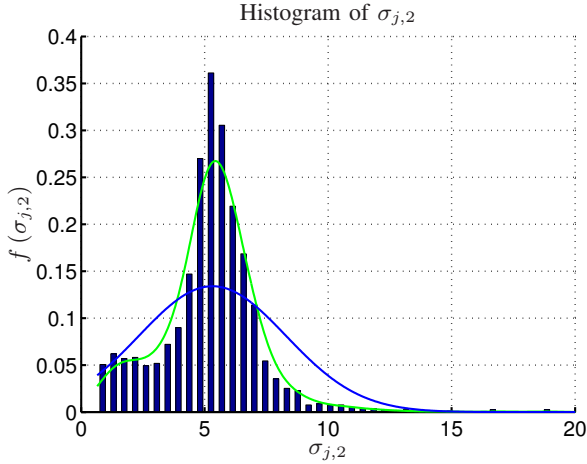


Fig. 15. Histogram of  $\sigma_{j,2}$ . The green curve shows a Gaussian kernel estimate [11] and the blue curve represents a Gaussian distribution having the same mean and variance as the data samples.

in motion with a speed of  $\approx 1$  m/s, two adjacent time pseudorange errors taken at 1 Hz are therefore uncorrelated.

## V. SUMMARY AND OUTLOOK

In this paper we described the temporal and spatial characterisation of measured pseudorange residuals for low cost receivers. The characterisation has been performed in terms of statistical analysis. While the spatial covariance function decays very fast over distance, a temporal dependence of the pseudorange error has been found. A second order AR process with samples drawn from a GMM(2) as driving noise has been proposed to model this dependence.

Future work will be done on integrating the results in recursive Bayesian filtering used for multisensor navigation.

## ACKNOWLEDGEMENT

This work was funded by the DLR internal project Galileo ADvanced APplications (GalileoADAP). The authors would like to thank Wei Wang and Patrick Robertson for their appreciated help and Teresa M. Martín Guerrero from the Institute of Communications Engineering at the University of Málaga for co-supervising Elena Abdo Sánchez's master thesis.

## APPENDIX

As described in Section III-A, Fig. 16 visualises another pseudorange error sequence  $\varepsilon_{j_1}(t)$  measured by a receiver located at  $P_5$ . In the same way as in Section III-A, Fig. 17 visualises the estimated driving noise  $\hat{v}_{j_1}(t)$  of the process  $\varepsilon_{j_1}(t)$ . Fig. 18 shows the sample covariance of  $\hat{v}_{j_1}(t)$  and Fig. 19 its histogram in comparison to the estimated pdf based on a GMM(2).

## REFERENCES

- [1] K. Wendlandt, P. Robertson, M. Khider, M. Angermann, and K. Sukchaya, "Demonstration of a Realtime Active-Tag RFID, Java Based Indoor Localization System using Particle Filtering," in *UbiComp*, Innsbruck, Austria, September 2007.

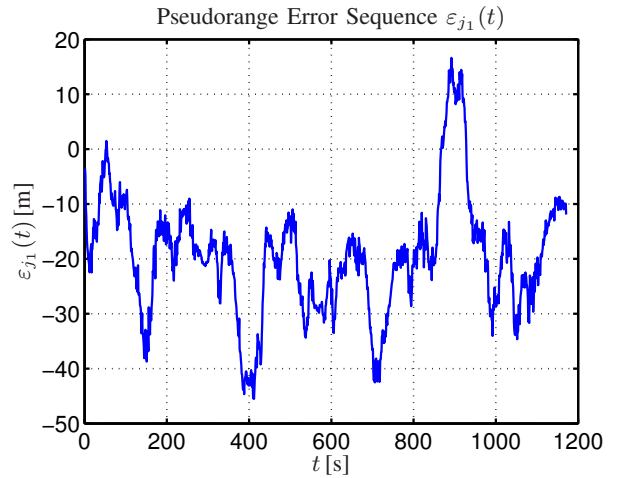


Fig. 16. Pseudorange error sequence  $\varepsilon_{j_1}(t)$  measured by a receiver located at  $P_5$ .

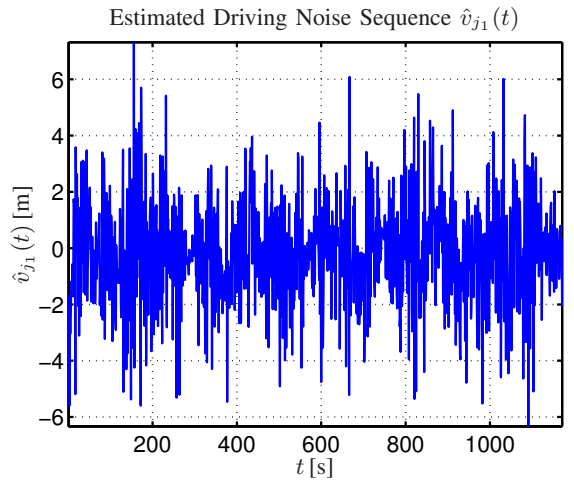


Fig. 17. Estimated driving noise sequence  $\hat{v}_{j_1}(t)$  by whitening the pseudorange error sequence  $\varepsilon_{j_1}(t)$  shown in Fig. 16 assuming a second order AR process for  $\varepsilon_{j_1}(t)$ .

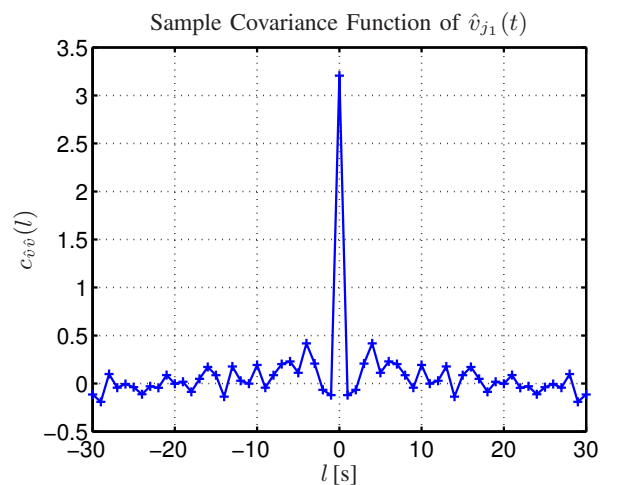


Fig. 18. Sample covariance function of  $\hat{v}_{j_1}(t)$  shown in Fig. 17.

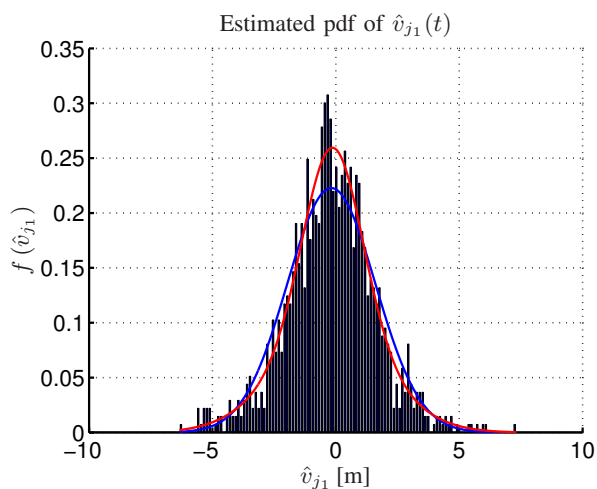


Fig. 19. Estimation of the pdf for  $\hat{v}_{j_1}(t)$  shown in Fig. 17. The blue curve visualises a Gaussian distribution having the same mean and variance as the data samples, while the red curve shows the parametric estimate based on a GMM(2).

- [2] T. King, T. Haenselmann, and W. Effelsberg, "Deployment, Calibration and Measurement Factors for Position Errors in 802.11-Based Indoor Positioning Systems," in *3rd Int. Symp., LoCA*, Germany, 2007.
- [3] B. Krach and P. Robertson, "Cascaded Estimation Architecture for Integration of Foot-Mounted Inertial Sensors," in *IEEE/ION PLANS*, Monterey, USA, May 2008.
- [4] M. Angermann, A. Friese, M. Khider, B. Krach, K. Krach, and P. Robertson, "A Reference Measurement Data Set for Multisensor Pedestrian Navigation with Accurate Ground Truth," in *ENC-GNSS*, Neapel, Italy, May 2008.
- [5] T. Jost and P. Robertson, "Statistical Characterisation of the Indoor Pseudorange Error using Low Cost Receivers," in *IEEE/ION PLANS*, Monterey, USA, May 2008.
- [6] B. W. Parkinson and J. J. S. Jr., *Global Positioning System: Theory and Applications, Vol. 1*. American Institute of Aeronautics and Astronautics Inc., 1996.
- [7] E. D. Kaplan, *Understanding GPS, Principles and Applications*. Artech House, 1996.
- [8] P. J. Duffett-Smith and A. R. Pratt, "Positioning with Punctured GPS," in *IEEE/ION PLANS*, Monterey, USA, May 2008.
- [9] S. Haykin, *Adaptive Filter Theory*. Prentice Hall, 1996.
- [10] S. M. Verbout, J. M. Ooi, J. T. Ludwig, and A. V. Oppenheim, "Parameter Estimation for Autoregressive Gaussian-Mixture Processes: The EMAX Algorithm," *IEEE Trans. on Sig. Processing*, vol. 46, no. 10, pp. 2744–2756, Oct. 1998.
- [11] B.W.Silverman, *Density Estimation for Statistic and Data Analysis*. Chapman and Hall, 1986.
- [12] P. J. Duffett-Smith, A. R. Pratt, T. Jost, and M. Kranz, "Positioning with Punctured GPS," in *Nav*, London, UK, Oct 2008.